Propagation of an intense Gaussian laser pulse in air*

John D. Reichert

Texas Tech University, Lubbock, Texas 79409

W. G. Wagner and W. Y. Chen

University of Southern California, Los Angeles, California 90007
(Received 18 November 1971; in final form 5 October 1972)

A numerical solution of the nonlinear macroscopic laser-fluid equations for propagation of a Gaussian laser pulse in air is described. The concept of "utility analysis" of numerical differencing schemes is introduced. With the computation scheme used, the laser pulse could be followed for only 10^{-5} sec; so enormous energy was put into the pulse to enhance the interaction with the fluid. Thus the initial pulse distortion could be observed. Analytical evaluation of the computer results produces a detailed quantitative check and suggests that a combination of analytic and numerical methods would allow a pulse to be conveniently followed for much longer periods of time. The preceding paper by the same authors describes various types of instabilities to be anticipated for propagation over long periods of time or with large powers.

I. INTRODUCTION

The work described in this paper was motivated by the discovery of instabilities in the system of equations describing electromagnetic wave propagation and fluid dynamics. These instabilities are described in the preceding paper.[1] A numerical solution of the full set of macroscopic laser-fluid equations (without saturation effects) is presented for a Gaussian laser pulse of enormous energy. The computation scheme employed was not optimal and the pulse could be followed for only 10^{-5} sec. Consequently, enormous energy was put into the pulse to enhance the laser-fluid interaction and drive the onset of strong distortions and instabilities.

Other computer solutions of the laser-fluid equations have recently been given[2] by various groups for physically reasonable powers. Such calculations have typically dealt with steady-state beams without saturation effects, but have included the effects of gravity. More recently saturation effects have been added and pulse shape is being considered.

In the course of these studies it became apparent that there was some merit to introducing a new concept to judge the value of an algorithm for computing the solutions of a system of partial differential equations. This concept was called "utility", and will be discussed only briefly in Sec. II. The full details will be published elsewhere.[3] The advantage of this concept is that it is relatively easy to apply to complicated systems of partial differential equations, whereas the stability concept leads to a very complicated procedure for deciding on the value of a numerical routine.

Speed and memory size in a computer place certain restrictions on one's ability to investigate phenomena in the laser-beam problem. In the attempt to calculate distortions of the type predicted by the linearized instability analysis, cylindrical symmetry was imposed on the problem in order to facilitate the computer calculation. Had this not been necessary, or had some other independent variable been eliminated rather than the angle about the beam axis, much more pronounced evidence of beam and fluid instabilities would likely have been observed for substantially lower powers, powers that may be achievable. Arguments supporting this proposition are contained in the preceding paper.[1]

In Secs. III and V we present the results of a calculation of beam distortion for a very high intensity pulse propagating through air for several kilomters. Analytical agruments are advanced in Sec. IV which suggest that the qualitative features of the distortions are correct, which lends credence to the computer output. Then, using the computer results as a check, the analytical procedure is shown to be adequate for detailed quantitative calculations. By combining the analytical procedure developed with appropriate computer support, the pulse could be followed much longer than the 10^{-5} sec described here.

II. DESCRIPTION OF THE PROCEDURE

The laser-fluid equations were solved in the near-field region of a laser pulse, initially Gaussian in both r and z, propagating through air at 1 atm of pressure and at 10 °C. A cylindrical geometry was used and cylindrical symmetry (no dependence on the angle ϕ) was preserved at the price of dropping the gravity term in the Navier-Stokes equation. Having cylindrical symmetry amounts to a considerable simplification in the problem, so that the inclusion of the free convection effects due to gravity was not attempted in this analysis. The problem described above amounts to a mixed initial-boundary problem. The initial configurations of the laser beam and the fluid are specified subject to certain boundary conditions at $r=0$ which must be satisfied at all times. Furthermore, the boundary condition at $z=0$ is time dependent, because the tail of the Gaussian must be fed into the spatial region. For the numerical solution, a spatial mesh of grid points or stations is used to represent the rz plane. At a given instant in time, the values of the various dependent variables are obtained at all of the stations. The difference equations are then employed with these values of the dependent variables to advance a step in time. This procedure is repeated over and over until the desired time interval has been traversed. An explicit difference scheme was used in this calculation, because such schemes are simplest to handle.

The two major difficulties in using numerical techniques to solve differential equations by computer are error growth and excessive computation time. In order to control the error growth, the utility criterion mentioned in Sec. I has been used. Furthermore, highly accurate

Copyright © 1973 American Institute of Physics

Downloaded 14 Sep 2009 to 163.13.32.114. Redistribution subject to AIP license or copyright; see http://jap.aip.org/jap/copyright.jsp

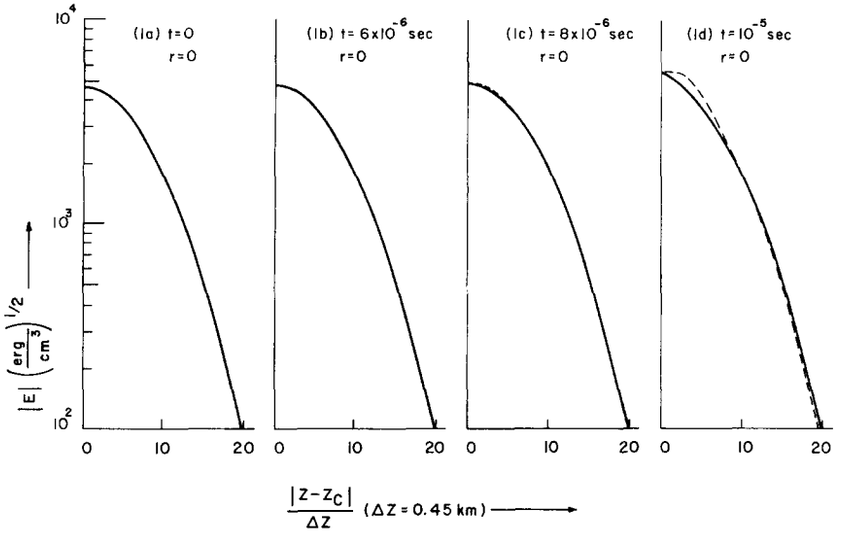

FIG. 1. On-axis magnitude of the electric field $|E|$ is shown as a function of $|z-z_c|$ at four different times. As shown in Eq. (16), $z_c \approx ct$ locates the "center" of the pulse. The solid curves show the leading edge of the pulse and the dotted curves depict the trailing edge. Distances along the z axis are expressed in units of the grid size: $\Delta z = 0.45$ km. The quantity $|E|$ shown is defined in Eq. (13), so that the exponential damping factor is not included in the graphs.

seven-point difference quotient representations of the differential operators were employed to reduce truncation error. In order to handle the economic problem of large computation time, a certain amount of efficiency is introduced by minimizing the amount of core storage required of the computer. This was accomplished in part by using overlaying techniques to store several pieces of information at the same site in the computer. Thus information is stored only as long as it is needed and then is replaced with current material. The computation time was also minimized by making use of a nonuniform grid. The seven-point difference relations allowed a relatively large grid size without undue truncation error and the nonuniform grid spacing permitted a greater grid density in the region of special interest. Thus an accurate solution could be obtained with a minimum of computation.

The laser-fluid equations are given in Eqs. (1)—(9) of Ref. 1. As mentioned above, the gravity term was dropped. Also, the thermal conductivity κ was taken to be constant because its derivatives are very small. The equation of state was taken to be the ideal gas law. The numerical values used for the various parameters are the same as those given for the linearized analysis in Ref. 1, because the same temperature and pressure were used for the undisturbed medium. The laser frequency ω_L and the dimensionless absorption constant α_0 were chosen to be 1.773×10^{14} sec^{-1} and 10, respectively. The wave equation for linearly polarized light in an absorptive medium is reduced to the scalar equation

$$c^2\nabla^2 E = \frac{\partial^2}{\partial t^2}(\epsilon E) + \alpha c \frac{\partial}{\partial t}(\sqrt{\epsilon}\, E). \tag{1}$$

This equation is an approximate equation describing an electric field which is polarized linearly. Strictly speaking, of course, Maxwell's equations do not allow cylindrically symmetric linearly polarized beams in charge-free space.

The solution of (1) is taken to be in the form

$$E = \tfrac{1}{2}(E_1 + iE_2)\exp i(\omega_L t - k_L z)\exp(-\tfrac{1}{2}\alpha z) + \text{c. c.}\,, \tag{2}$$

where E_1 and E_2 are slowly varying functions of $\mathbf{r}$ and t and the laser frequency and wave number are related by

$$\epsilon_{0e}\omega_L^2 = c^2 k_L\,, \tag{3}$$

where ϵ_{0e} is defined in Eq. (11) of Ref. 1. Equation (2) was substituted into (1) and the second derivatives of E_1 and E_2 with respect to time were dropped. From the real and imaginary parts of the resulting equation, coupled simultaneous differential equations for E_1 and E_2 were obtained. These equations are also coupled to the differential equations for ρ, T, and the cylindrical components v_r and v_z of the fluid velocity. The use of cylindrical symmetry allows the simplification $v_\theta = 0$.

The easiest way to obtain a variable grid size is to introduce a transformation to a new indpendent variable. Thus, in order to have more grid points in the region of special interest, small r, the nonlinear transformation

$$r/r_0 = x/(1-x) \tag{4}$$

was employed. The scale value r_0 was chosen according to the dictates of convenience and will be shown in Eq. (9).

Because of the symmetry of the problem and the regularity of the differential equations, the following boundary conditions must be satisfied at $x=0$:

$$\frac{\partial E_1}{\partial x} = \frac{\partial E_2}{\partial x} = \frac{\partial T}{\partial x} = \frac{\partial \rho}{\partial x} = \frac{\partial v_z}{\partial x} = \frac{\partial v_r}{\partial z} = \frac{\partial^2 v_r}{\partial z^2} = v_r = 0$$

$$\frac{\partial^2 v_r}{\partial x^2} = 2\frac{\partial v_r}{\partial x}\,. \tag{5}$$

The laser-fluid differential equations must, of course, be converted to difference equations before a computer solution can be attempted. As indicated earlier, seven-point difference quotients were used to represent the differential operators, but these difference quotients will not be presented. (The scheme was a straightforward explicit difference representation.)

Once the difference equations have been written, it is vital to have some criterion to determine useful time step sizes and corresponding grid spacings. It is not, however, necessary to demand that the difference scheme be stable in the classical sense. In fact, the classical notion of stability is irrevelant to computer solution of differential equations, particularly for non-

Downloaded 14 Sep 2009 to 163.13.32.114. Redistribution subject to AIP license or copyright; see http://jap.aip.org/jap/copyright.jsp

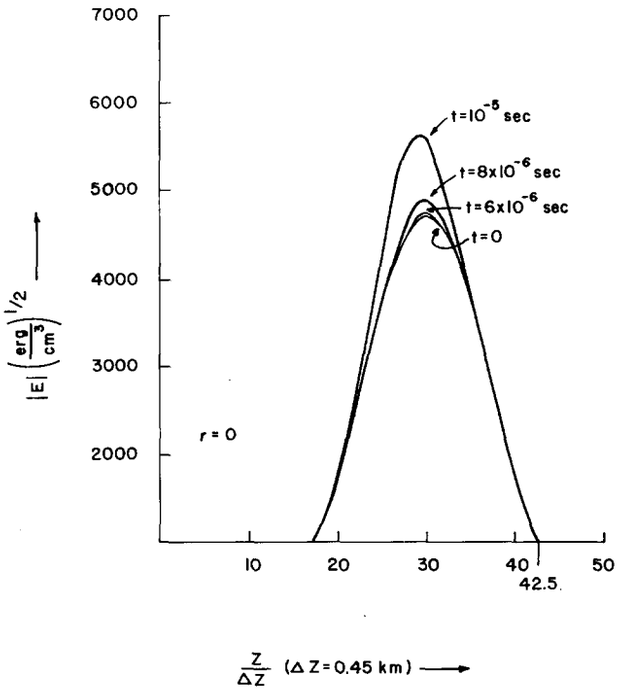

FIG. 2. For detailed comparison, the z profile of the on-axis electric field $|E|$ is shown at several times. The unit Δz is used for distances along the z axis. The curves have been displaced to the left and the leading edges made to coincide at height 1000 $(\text{erg/cm}^3)^{1/2}$ for $|E|$. The abscissa for this intersection of the curves has been labeled 42.5, the location of this point at $t=0$.

linear systems. This argument is presented in detail in another paper[3] and another kind of criterion, "utility", is proposed. A difference scheme is "useful" for prescribed ϵ and N if the computer solution of the scheme produces results for N time steps which differ in magnitude from the correct solution of the original differential equations by an amount less than ϵ. Thus, utility analysis is totally different in philosophy than stability and, incidentally, is far easier to apply. A number of theorems have been developed which allow rapid and powerful assessment of the utility regions of differencing schemes of all types. Because these matters would only extend the length of the present paper and because it is believed that utility procedures will be worthwhile in a broader context than the problem at hand, a separate paper is devoted to the subject and only a brief sketch of the analysis will be given here.

It turns out that a utility region for an explicit differencing scheme can be determined from a relation of the form

$$\Delta t < [(4\bar{\delta})(\tfrac{1}{100}N)]^{-1}, \tag{6}$$

where Δt is the time step size, N is the number of time steps to be made, $\epsilon \sim 10^{-5}$, and $\bar{\delta}$ is a function of the spatial mesh sizes and is determined from the differencing scheme. For the seven-point explicit difference scheme used to represent the laser-fluid system, $\bar{\delta}$ is trivially determined to be[3]

$$\bar{\delta} \approx c[3/k_L(r_0\Delta x)^2 + 2/\Delta z], \tag{7}$$

so that the utility restriction predicted is

$$1/c\Delta t \geq 12/k_L(r_0\Delta x)^2 + 8/\Delta z. \tag{8}$$

Since $\bar{\delta}$ is given only approximately by (7), the laser power I_L does not appear. The differencing scheme employed was not optimal and its utility region is entirely dominated by the electric field development and is insensitive to the fluid parameters. This was, however, the scheme employed in the present solution.

Condition (8) is such a strong constraint that one immediately wonders if it is really necessary to obey it. Part of the utility philosophy is to obtain a constraint like (8) and try it on the computer. Then one can try to violate the condition, using a larger Δt, and compare the results. This was done for the problem discussed in this paper and no escape from (8) was possible for the difference scheme used. In fact, if the criterion was violated by a factor of order 5 in Δt, then classic instability phenomena were observed in the computer output. Thus, by a stroke of bad luck, it appears that (8) must be obeyed.

In order to emphasize the implications of (8) for the study of the propagation of laser pulses, a description of the accessible parameter regime will now be given.

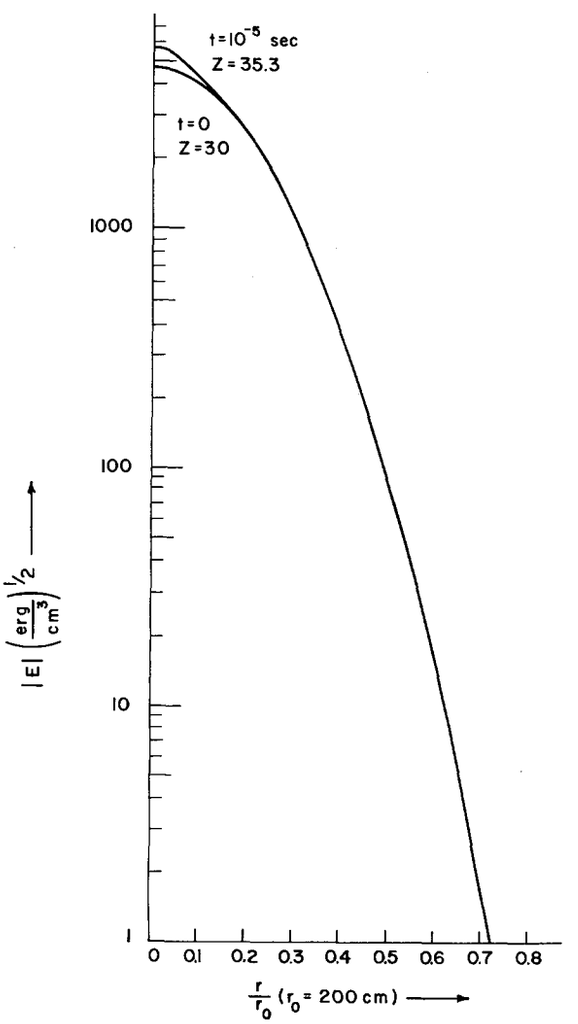

FIG. 3. Radial profile of $|E|$ is shown for $t=0$ and for $t=10^{-5}$ sec for slices taken through the on-axis maximum z_p in the z profile.

Downloaded 14 Sep 2009 to 163.13.32.114. Redistribution subject to AIP license or copyright; see http://jap.aip.org/jap/copyright.jsp

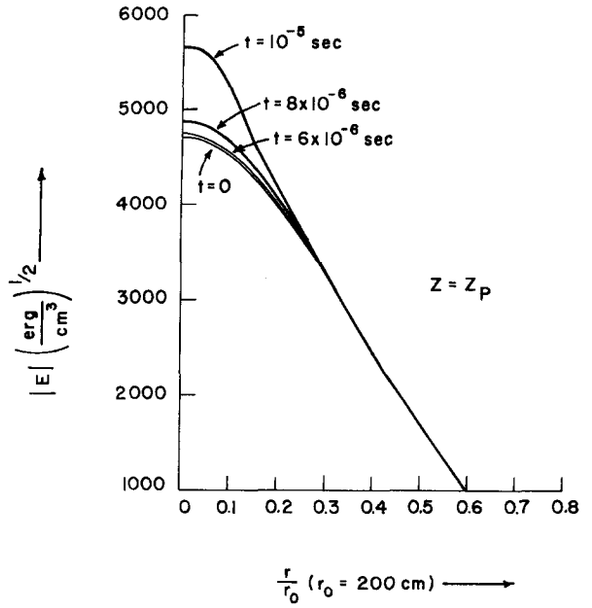

FIG. 4. Details of the radial profile are shown for various times. In all four cases the radial slice through the on-axis maximum of the z profile is exhibited.

As a starting point for this discussion, the parameter values used in the actual calculation will be listed. The electric field at $t=0$ was taken to be of the form

$$E_1 = F\exp[-4(r/r_0)^2]\exp\{-4[(z-z_{p0})/z_0]^2\},$$
$$E_2 = 0, \tag{9}$$

where

$r_0 \equiv$ full $(1/e)$ width of $E_1(r, z=z_p, t=0)$
$\equiv \sqrt{2}$[full $(1/e)$ width of I_L at $z=z_{p0}$, $t=0$];

$I_L \equiv$[on-axis intensity (in erg/cm² sec) at $r=0, z=z_{p0}$, $t=0$, time averaged over several optical periods]
$\equiv \frac{1}{2}(\epsilon_{0e})^{1/2}cF^2$;

$z_0 =$ full $(1/e)$ width of $E_1(r=0, z, t=0)$.

$z_{p0} =$ location of the peak at $t=0$;

$$F^2 = \frac{2I_L}{(\epsilon_{0e})^{1/2}c} \equiv \frac{16P_L}{(\epsilon_{0e})^{1/2}cr_0^2} \equiv \frac{64\,U}{\pi(2\pi)^{1/2}\epsilon_{0e}r_0^2 z_0} \tag{10}$$

$=$ peak value of the electric field, squared;

$P_L =$ total power (in erg/sec) of the pulse at $z=z_{p0}$, $t=0$, time averaged over several optical periods;

$U =$ total energy in the pulse at $t=0$, time averaged over several optical periods.

The values taken for these quantities were

$$r_0 = 200 \text{ cm},$$
$$z_0 = 9\times10^5 \text{ cm} = 9 \text{ km},$$
$$z_{p0} = 13.5\times10^5 \text{ cm} = 13 \text{ km},$$
$$F = 4.7\times10^3 \text{ (erg/cm}^3)^{1/2}, \tag{11}$$
$$I_L = 3.3\times10^{17} \text{ erg/(cm}^2 \text{ sec)},$$
$$P_L = 5.2\times10^{21} \text{ erg/sec},$$
$$U = 9.8\times10^{16} \text{ erg},$$

and the air was taken to be initially in its unperturbed state at 1 atm pressure and at 10 °C. The reason for these astronomical powers will be explained later.

The spatial grid was composed of $80\times16=1280$ mesh points. The z axis was evenly divided into 80 steps of size $\Delta z = 0.45\times10^5$ cm $= 0.45$ km beginning at $z=0$ and extending to $z=35.6\times10^5$ cm $=35.6$ km. Thus the peak of E_1 was initially located at the 30th mesh point on the z axis and its $1/e$ width extended from the 20th to the 40th mesh point. The radial variable x has the range $0\le x\le 1$ and this range was evenly divided into 22 steps of size $\Delta x = \frac{1}{22}$, but only the 16 sites closest to the z axis were used. The more distant sites correspond to radial distances greater than five beam half-widths. The first step away from the z axis corresponds to the radial distance $\Delta r = 200$ cm$/21 = 9.5$ cm $\approx \frac{1}{10}\times$(radial half-width). The time step size was taken to be $\Delta t = 10^{-7}$ sec and 100 steps were made so that the time interval $0\le t \le 10^{-5}$ sec was traversed.

Taking these grid sizes and time steps and subtituting into the utility condition (8), one gets

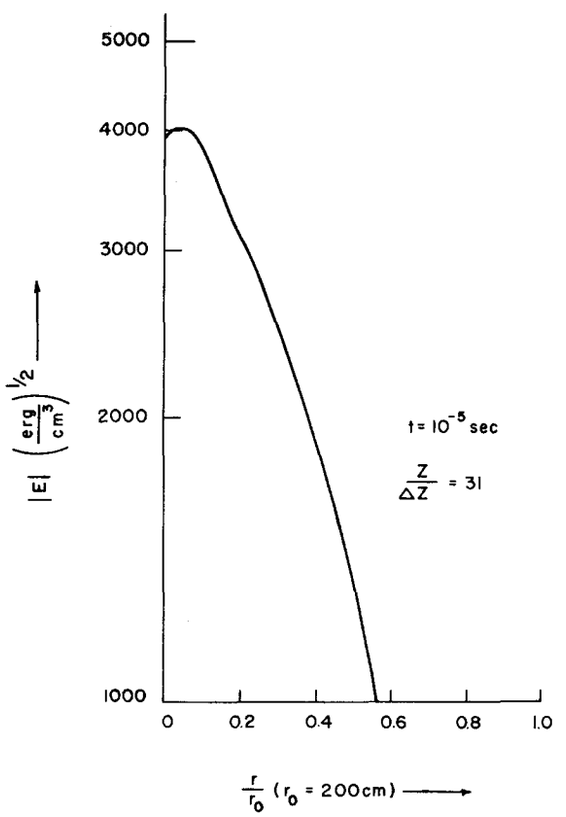

FIG. 5. An off-axis maximum in the radial profile is shown at $t=10^{-5}$ sec. The slice shown exhibits the radial profile at $z=31$, whereas the principal peak of the pulse is on axis at $z=35.3$. The slice at $z=31$ contains the greatest off-axis effect and, therefore, locates the two secondary peaks which have developed in the pulse. These secondary peaks are also indicated on Fig. 9.

Downloaded 14 Sep 2009 to 163.13.32.114. Redistribution subject to AIP license or copyright; see http://jap.aip.org/jap/copyright.jsp

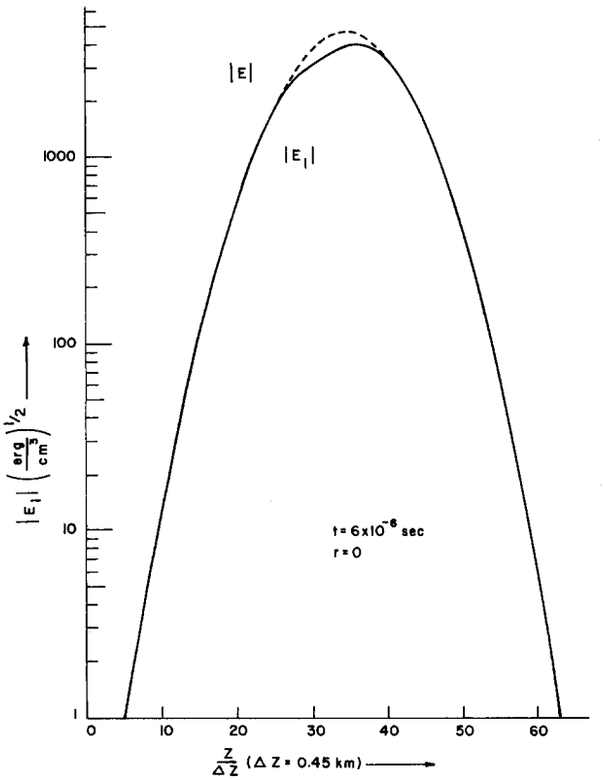

FIG. 6. Phase information is presented by showing $|E_1|$ as a function of z at $t=6\times10^{-6}$ sec. For comparison, the dashed curve shows $|E|$. Equations (2) and (13) of the text define $|E_1|$ and $|E|$.

$$\frac{1}{c\Delta t}=\frac{1}{3000}\geq\frac{1}{40\,800}+\frac{1}{5630}$$

$$=12/k_L r_0^2(\Delta x)^2+8/\Delta z\,. \qquad (12)$$

Thus, for the chosen step size Δz, the value used for Δt would violate the condition, were it to be doubled. Of course, the condition (8) is only approximate, but, as mentioned above, good solutions could not be obtained for $\Delta t\sim10^{-6}$ for $\Delta z=0.45$ km. Clearly the value $\frac{1}{22}$ used for Δx does not saturate the Δx piece of (12) and one could probably use Δx as small as $\frac{1}{60}$. Such a small step size for Δx would, however, require three times as many spatial mesh points and would exceed the storage capacity of the computer which was used.

The desire is to use as large a value of Δt as one can. In this regard, the Δx piece of (12) is generous and would permit $\Delta t\sim10^{-6}$. The z step size would have to be increased to $\Delta z\sim5$ km to allow this, however. Such a large step size would be larger than the 4.5 km half-width of the pulse selected, so that no details of deformation of the pulse could be observed.

If the beam is made narrower in radial extent, the Fresnel length decreases and diffraction effects become important. The Fresnel length is 310 km for $r_0=200$ cm, so that one would become involved with far-field effects if the beam radius were decreased by more than a factor of 5. Making the pulse longer in the z direction expands the time scale over which interesting effects may be studied. If, on the other hand, the pulse is shortened in the z direction, then one must shift to smaller values of Δz in order to be able to follow details of the development of the pulse. Shifting to smaller Δz requires, because of (12), that one use smaller values of Δt. The net effect is that no profit is derived from using shorter pulses, because they can be followed only for correspondingly shorter times.

One aspect of the parameter regime has not yet been discussed: the range of power for the beam. Since the power I_L does not appear in the utility criterion, its role must be determined by experimentation with the computer program. Very small powers are not interesting because there is very little interaction with the fluid. In order to see instabilities and nonlinear effects during short times, one would wish to consider beams with large power densities. The extremely large values shown in (11) produce interesting effects, in a time interval of 10^{-5} sec. Such beams cannot be followed for more than about 100 time steps, however, because the various dependent variables begin to develop large curvatures and vary on a scale smaller than the mesh sizes. Thus if one wishes to follow the development for a long period of time, the mesh sizes must be decreased and eventually the time step will have to be smaller, and then many more time steps will be required. In this regard, one must keep in mind that if the mesh size is decreased, while the initial pulse size is not decreased, then more mesh points will be required and the storage capacity of the computer also becomes a limiting factor.

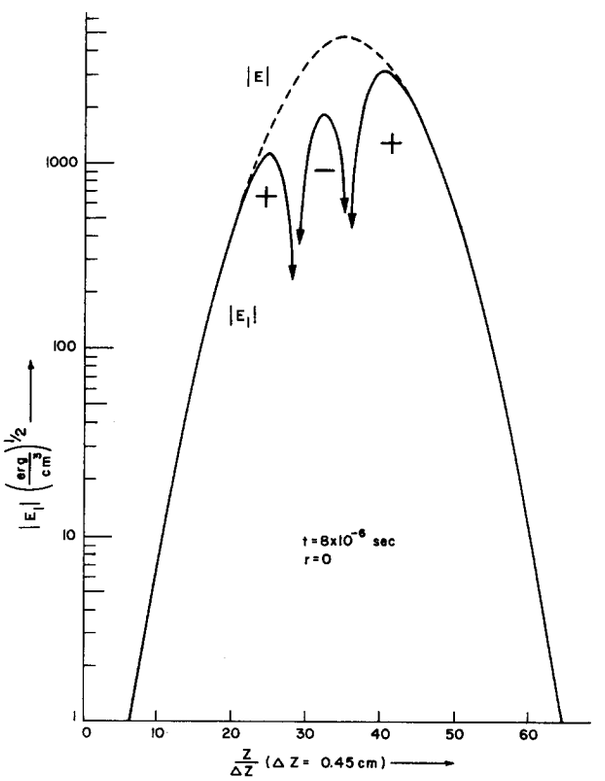

FIG. 7. At $t=8\times10^{-6}$ sec, $|E_1|$ and $|E|$ are shown on axis as functions of z. Two nodes have developed and E_1 is negative in the region of the power peak. The sign of E_1 in the various regions is indicated on the figure. The nodes are also shown in Fig. 9.

Downloaded 14 Sep 2009 to 163.13.32.114. Redistribution subject to AIP license or copyright; see http://jap.aip.org/jap/copyright.jsp

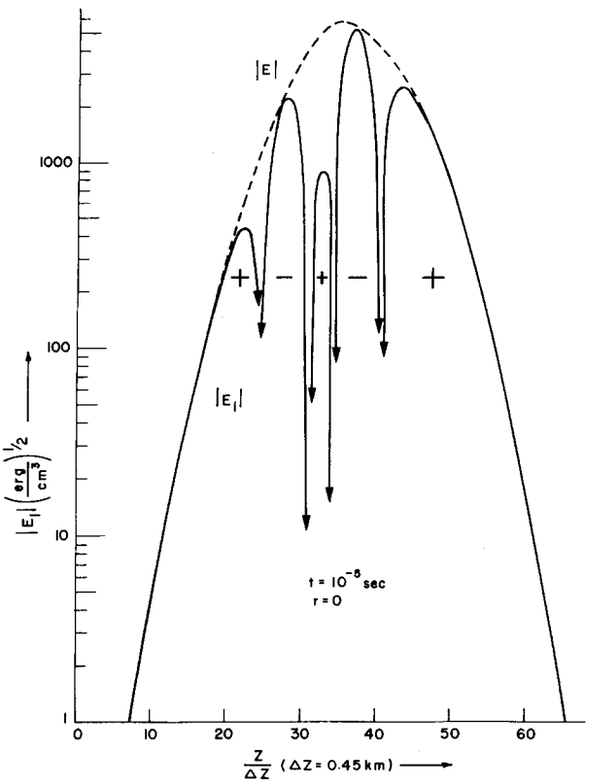

FIG. 8. At $t=10^{-5}$ sec, $|E_1|$ and $|E|$ are shown on axis as functions of z. The sign of E_1 is indicated in the various regions. There are now four nodes. The nodal curves are phase fronts and are shown in detail in Fig. 9.

The final remaining option is to increase the power in the beam even more. The net effect is that the large curvatures develop faster and the development can be followed only for shorter periods of time.

One final remark about numerical solution of the laser-fluid equations will be made before discussing the results of the computer calculation. Strong growth, instabilities, and nonlinear effects, can often not be followed because of the mesh sizes employed. If these strong oscillations or secular growths are generated by tiny rapidly changing terms, that is, if the instabilities arise due to ripple effects which become strongly enhanced, then a crude mesh size can smooth these effects out and, thereby, prohibit the occurrence of the strongly growing phenomena by removing their source. Very strong instabilities were found in Ref. 1 for the linearized laser-fluid equations. The strongest of these instabilities are generated by very short wavelength ripple. The mesh size employed in the present calculation will begin to wash out ripple about an order of magnitude larger in wavelength than the ripple which is most strongly amplified in the linearized analysis. Thus, one must bear in mind that some physical sources of pulse distortion will be excised by the mesh selected.

Accepting the many restrictions noted above, we have examined the propagation of a 200-cm by 9-km pulse with 10^{17} erg for 10^{-5} sec. The pulse moves 3 km during this time and it is possible to observe the onset of the laser-fluid interaction in some detail.

III. RESULTS OF THE COMPUTATION FOR THE ELECTRIC FIELD

The results of the calculation are presented in Figs. 1–17. The electric field is conveniently considered in terms of the quantity

$$|E| \equiv (E_1^2 + E_2^2)^{1/2}, \tag{13}$$

where E_1 and E_2 are the slowly varying electric amplitudes defined in (2). The instantaneous electric field is thus given by

$$E = |E| \cos(\omega_L t - k_L z + \delta_E), \tag{14}$$

where the phase δ_E is given by

$$\delta_E = \tan^{-1}(E_2/E_1).$$

As shown in (9), at $t=0$, E_2 is taken to be zero and, consequently, δ_E is zero initially. Thus

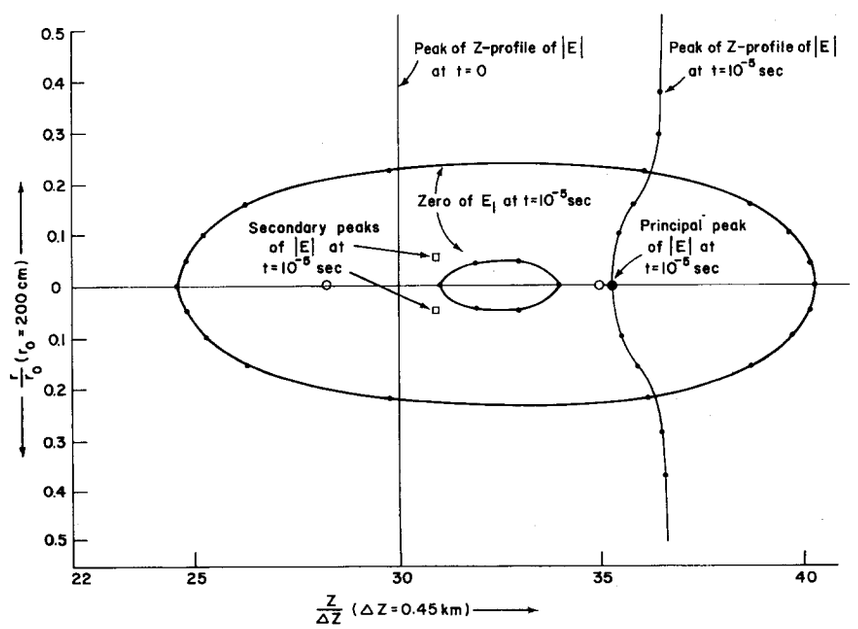

FIG. 9. Various properties of the pulse are shown in the rz plane. The location of the peak in the z profile is shown as a function of r at $t=0$ and at $t=10^{-5}$ sec. The phase fronts with $E_1=0$ are shown at $t=$ $t=10^{-5}$ sec. The open circles locate the z-profile nodes of E_1 at $t=8\times10^{-6}$ sec. The small squares locate the secondary maxima of the pulse at $t=10^{-5}$ sec.

Downloaded 14 Sep 2009 to 163.13.32.114. Redistribution subject to AIP license or copyright; see http://jap.aip.org/jap/copyright.jsp

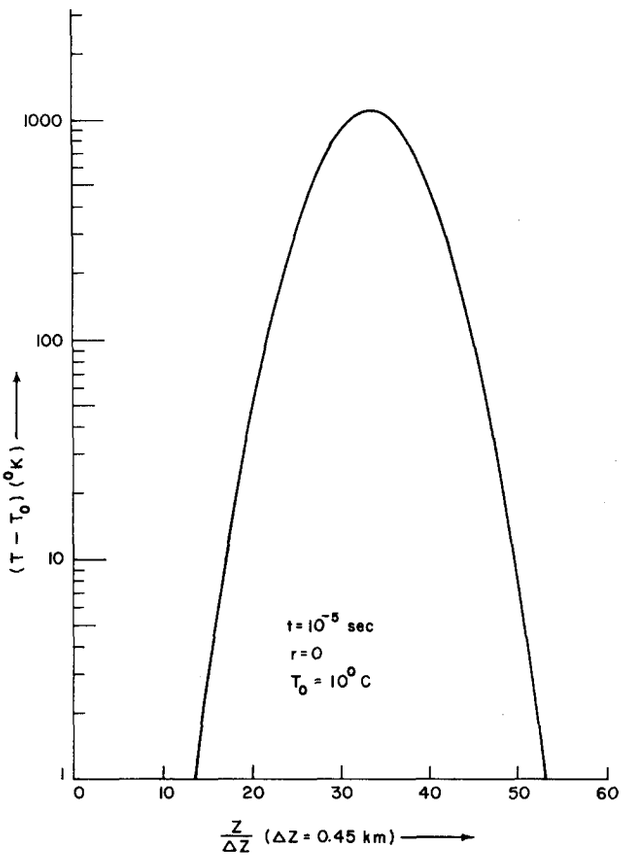

FIG. 10. On-axis temperature increment $T - T_0$ is shown as a function of z at $t = 10^{-5}$ sec.

$$|E| = E_1 \quad \text{at } t = 0, \tag{15}$$

and E_1 is described by Eqs. (9)—(11) initially. This initial pulse shape in exhibited in Figs. 1(a) and 3.

In Fig. 1 the z profile of the pulse is shown at the initial time, at 10^{-5} sec, and at two intermediate times. For $t \neq 0$, the pulses are not absolutely symmetric about their peaks. In order to exhibit this asymmetry, the curves are plotted as a function of $|z - z_c|$, where z_c is the center of the pulse. This device allows direct comparison of the leading and trailing edges of the pulses. The center z_c is defined to be the point equidistant from the leading and trailing edges at $|E| = 1$ (erg/cm^3)$^{1/2}$. These values are (t in sec)

$$\begin{array}{llll} t=0 & t=6\times10^{-6} & t=8\times10^{-6} & t=10^{-5} \\ z_c=30 & z_c\approx34 & z_c\approx35.3 & z_c\approx36.6, \end{array} \tag{16}$$

where for convenience, distances along the z axis will be given in units of grid size: $\Delta z = 0.45\times10^5$ cm $= 0.45$ km. One notes, therefore, from (16) that this pulse center propagates at the velocity $v_c \approx 2.97\times10^{10}$ cm/sec, the velocity of light. The pulse peaks, however, are observed to drift backward with respect to z_c (t in sec):

$$\begin{array}{llll} t=0 & t=6\times10^{-6} & t=8\times10^{-6} & t=10^{-5} \\ z_p\approx30 & z_p\approx34 & z_p\approx35.2 & z_p\approx35.3, \end{array} \tag{17}$$

so that after 10^{-5} sec, the peak has lost about $\frac{2}{3}$ km with respect to z_c. Note that the exponential damping factor shown in (2) is not included in the quantity $|E|$ appearing in the graphs. For air, this factor is larger than 0.95, even at $t = 10^{-5}$ sec. Other than this effect, very little energy is lost from the beam due to heating of the fluid, so the distortion effects shown in Fig. 1 are rather minor and are noticeable only near the peak of the pulse. Extra detail of this peak distortion is shown in Fig. 2. For purposes of this display, the leading edges have been placed together so that the curves intersect at $|E| = 10^3$ (erg/cm^3)$^{1/2}$ and the corresponding abscissa has been labeled 42.5, the location of this point at $t = 0$. The retrograde peak motion and the corresponding loss of fore and aft symmetry in the vicinity of the peak are plainly seen.

The radial beam profile is exhibited in Figs. 3 and 4. The radial slice shown at each value of the time is taken through the position of the maximum z_p in the z profile. In Figs. 3 the entire beam profile is shown for the initial and final times only. Comparison of the curves reveals a small on-axis increase extending out to the beam half-width (half of the full $1/e$ width) at $\frac{1}{2}r_0 = 100$ cm. The effect amounts to a 47% increase in the on-axis intensity. Details and intermediate states are given in Fig. 4.

Although it may appear from Figs. 1—4 that the energy in the pulse is not conserved properly and that the beam is gaining energy, such is not the case. The total energy in the pulse is in fact constant to within 5% throughout

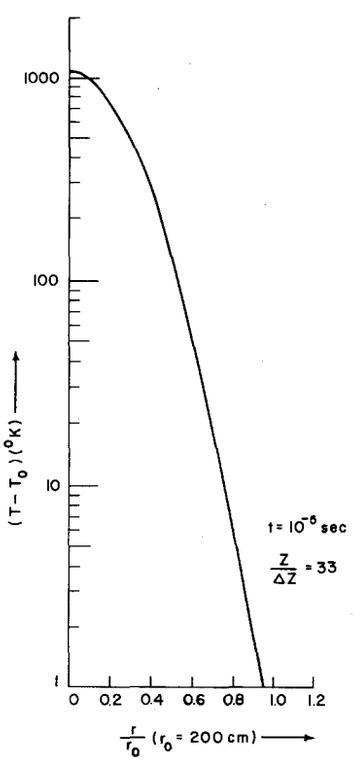

FIG. 11. Radial profile of the temperature increment is shown at $t = 10^{-5}$ sec for the slice through the maximum of the z profile. This maximum is at $z = 33$ as may be seen in Fig. 10.

Downloaded 14 Sep 2009 to 163.13.32.114. Redistribution subject to AIP license or copyright; see http://jap.aip.org/jap/copyright.jsp

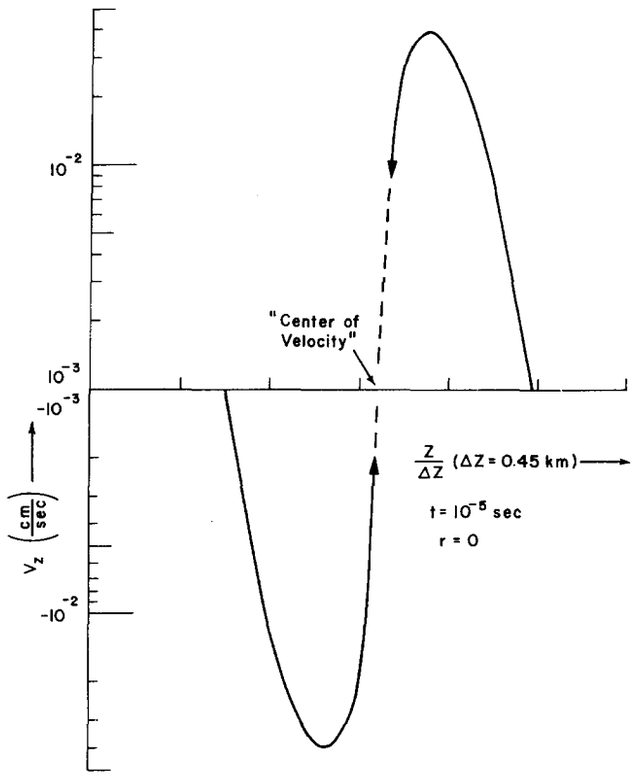

FIG. 12. z component v_z of the fluid velocity is shown on axis as a function of z at $t=10^{-5}$ sec. A double log plot is used which omits values of v_z between 10^{-3} and -10^{-3} cm/sec.

the computer calculation. The shape of the pulse is merely becoming slightly more complicated. Although the radial peak is on axis in the slice through the peak in the z profile, this is not the case for slices taken behind z_p. For example, at $t=10^{-5}$ sec, the principal peak is at $z_p \approx 35.3$. As one moves away from this peak toward the trailing edge, the radial peak moves off axis giving a maximal effect near $z=31$. The principal peak of the pulse is, however, always on axis. The radial profile at $z=31$ is shown in Fig. 5. This is clearly only a small detail at $t=10^{-5}$ sec. The position of this off-axis secondary peak is also located in Fig. 9 and marked with tiny squares.

In order to follow the development of the phase of the electric field, the quantity $|E_1|$ is plotted in Figs. 6–8, for $t \neq 0$. Of course, at $t=0$, $|E_1|=|E|$ and the phase δ_E is zero. In these three figures the graph of $|E|$ is marked with dotted lines for comparison. The corresponding value of $|E_2|$ can be deduced from these figures, using (13). These figures show far more dramatic effects than the curves discussed above. At $t=6\times10^{-6}$ sec, the phase is still nearly zero and E_1 is positive everywhere. At $t=8\times10^{-6}$ sec, however, E_1 has changed sign over a 3-km region extending from slightly in front of the peak of $|E|$ toward the trailing edge of the beam. This is clear-cut evidence of the onset of laser-fluid interaction in the trailing edge of the beam. It is clear that the front of the pulse and the distant tail are, as yet, unaffected by this interaction. It is interesting that the unperturbed part of the leading edge does not reach as far back as the principal peak. Thus, the peak already feels the effects of the interaction to some degree and comparison of (16) and (17) reveals that the peak will now begin to lose ground with respect to the center of the pulse. This effect has already been noted in the graphs of $|E|$.

Since there are now places where $|E_1|$ is zero, it is clear that the phase goes to $\frac{1}{2}\pi$ at these sites. The amplitude E_2 responds strongly at those places where $E_1=0$, fulfilling the obligation to conserve power. One notes that the graph of $|E|$ remains very smooth, giving no indication that the phase is varying rapidly. Figure 8 shows the later development of the region in which E_1 changed sign. The region in which $E_1<0$ is now 7 km long, nearly as large as the $1/e$ width of $|E|$. This region has advanced now to a point well in advance of the principal peak and extends back far into the tail. It appears that this node is propagating forward at nearly four times the speed of light. Furthermore, there has been another sign reversal of E_1 slightly behind the peak. It is this kind of oscillatory behavior in E_1, with large variations on the scale of the chosen mesh size, that brings a halt to further observation of the beam development by this method.

On the rz plane shown in Fig. 9, the constant phase curve $E_1=0$ is shown in detail at $t=10^{-5}$ sec. Also marked, with small open circles, is the on-axis extent of the similar curve at $t=8\times10^{-6}$ sec, encountered in Fig. 7. Also indicated on the same figure is the locus of maxima in the z profile of the pulse for off-axis slices, both at $t=0$ and $t=10^{-5}$ sec. At $t=0$, the pulse is described by (9) and clearly the off-axis slices all have maxima in z positioned at $z_{p0}=30$. As the pulse propa-

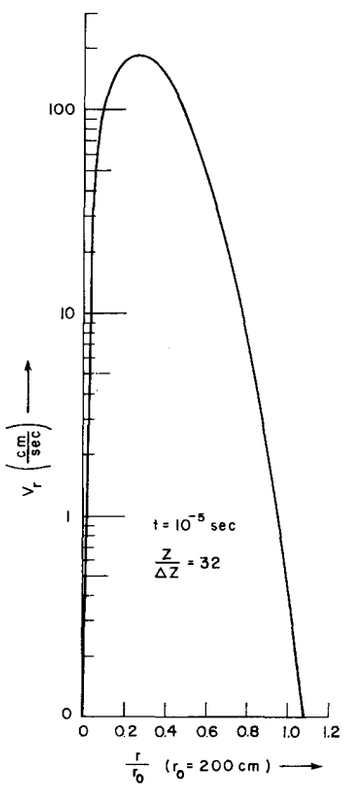

FIG. 13. Radial component v_r of the fluid velocity is shown as a function of r at $t=10^{-5}$ sec. The slice is taken at $z=32$, the location of the "center of velocity" shown in Fig. 12.

Downloaded 14 Sep 2009 to 163.13.32.114. Redistribution subject to AIP license or copyright; see http://jap.aip.org/jap/copyright.jsp

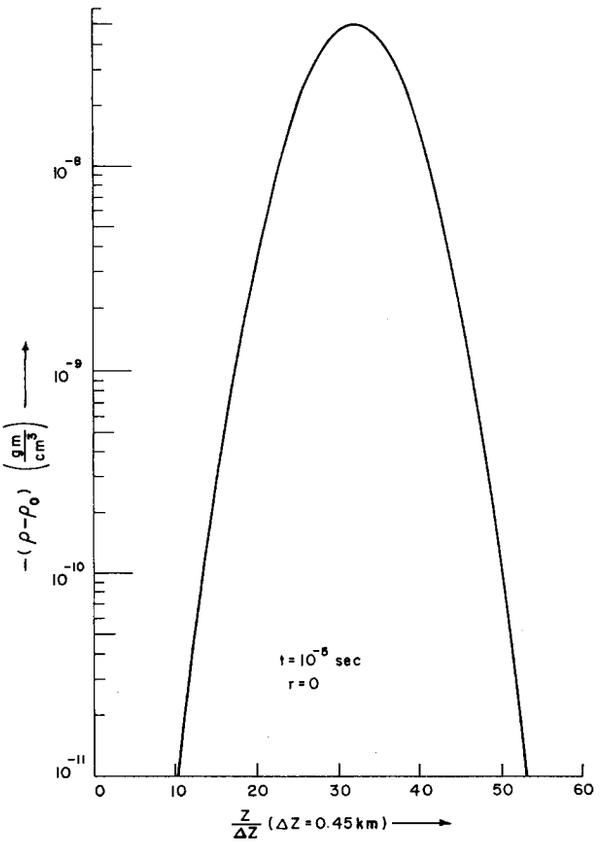

FIG. 14. On-axis fluid density decrement, $-(\rho-\rho_0)$, is shown as a function of z at $t=10^{-5}$ sec.

gates, however, the peak moves slower than the velocity of light, as previously noted. The off-axis portions of the pulse, however, have much smaller intensity and, consequently, interact very little with the fluid. These portions of the pulse will suffer no delay, and move steadily ahead of the principal peak. One notes that at two-thirds of the radial half-width of the beam, the delay has disappeared almost completely. As mentioned above, the small squares locate the secondary peaks present at $t=10^{-5}$ sec.

IV. ANALYTICAL PROCEDURE DEVELOPED TO EVALUATE AND EXTEND THE CALCULATION

The phase-front information presented in Figs. 6–9 is an interesting feature of the results of the computer solution. Since $|E_1|$ turns out to be a rapidly varying function of time, it is of interest to attempt to understand the mechanism responsible for the behavior of E_1. In order to understand this behavior, one must realize that the phase depends on the state of the fluid. The state of the fluid given by the computer calculation is shown in Figs. 10–16. Before these figures are discussed, however, it is convenient to examine certain analytic estimates for the fluid variables. Such estimates will allow insight into the behavior of E_1 and, later, will facilitate the discussion of the computer results for the fluid variables.

In order to describe the behavior of E_1, it is useful to write the electric field in the form

$$E=\mathcal{E}_0(r,z-ct)\exp\{i[\omega_L t-(\sqrt{\epsilon}\,\omega_L/c)z]\}+\text{c. c.}\,, \tag{18}$$

where

$$\mathcal{E}_0\equiv\tfrac{1}{2}F\exp[-4(r/r_0)^2]\exp\{-4[(z-ct)/z_0]^2 \tag{19}$$

and

$$\sqrt{\epsilon}\approx 1+[(\epsilon_0-1)/2\rho_0]\rho_1\,, \tag{20}$$

where F is a slowly varying amplitude, $\rho_1=\rho-\rho_0$ is the local density excess, and for the present considerations z_{p0} has been put equal to zero. Combining Eqs. (18)–(20), the electric field can be put in the form shown in (2) with

$$E_1=\left[F\cos\left(k_L z\frac{\epsilon_0-1}{2\rho_0}\rho_1\right)\right]\exp\left[-4\left(\frac{r}{r_0}\right)^2\right]\exp\left[-4\left(\frac{z-ct}{z_0}\right)^2\right], \tag{21}$$

$$E_2=\left[-F\sin\left(k_L z\frac{\epsilon_0-1}{2\rho_0}\rho_1\right)\right]\exp\left[-4\left(\frac{r}{r_0}\right)^2\right]\exp\left[-4\left(\frac{z-ct}{z_0}\right)^2\right].$$

These expressions agree with (9) at $t=0$ and offer a way estimate the behavior of E_1 at subsequent times. On the basis of (21) the nodes of E_1 might be expected to be determined by

$$\cos\{k_L z[(\epsilon_0-1)/2\rho_0]\rho_1\}=0\,. \tag{22}$$

Actually, this expression should be modified slightly if one wishes to attempt to get quantitative agreement with the computer solution. It is clear that (21) requires E_2 to vanish at $z=0$ at all times. This is not the same boundary condition which was used in the computer solution. Actually one should use

$$E_1\sim\cos\psi$$

with

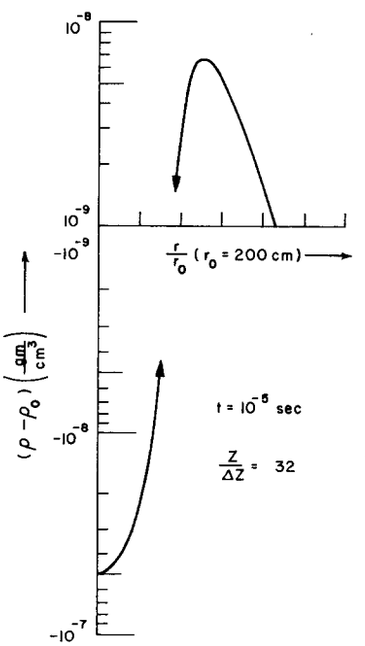

FIG. 15. Radial density distribution is exhibited as a function of r at $t=10^{-5}$ sec. The slice is taken at $z=32$, the location of the density minimum detailed in Fig. 14. A double log plot is used which omits values between 10^{-9} and -10^{-9} g/cm^3.

Downloaded 14 Sep 2009 to 163.13.32.114. Redistribution subject to AIP license or copyright; see http://jap.aip.org/jap/copyright.jsp

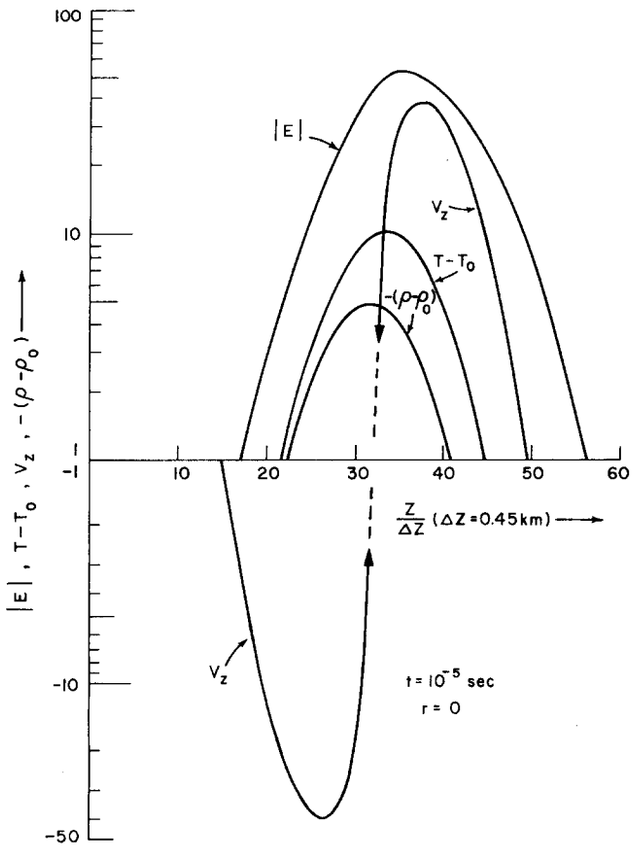

FIG. 16. On a double log plot, the various laser and fluid variables are simultaneously plotted versus z at $t=10^{-5}$ sec so that the spatial location of the various pulses can be visualized.

$$\psi = k_L \int_{z-ct}^{z} \{[(\epsilon_0 - 1)/2\rho_0]\,\rho_1\}_{z',t'}\, dz' \,. \tag{23}$$

The integrand in (23) should be evaluated at z' and t', where

$$c(t'-t) = z'-z.$$

It is clear from (21) and (23) that the mechanism responsible for the behavior of E_1 is easily exhibited. To actually follow the behavior of E_1, however, it is clearly necessary to determine the state of the fluid. In particular, the density excess ρ_1 must be obtained as a function of time and position. In order to analytically describe the fluid for the time interval and parameter ranges of the computer solution, the laser-fluid equations may be simplified to

$$\rho_0 \frac{\partial T_1}{\partial t} \approx \frac{\gamma-1}{\beta}\frac{\partial \rho_1}{\partial t} + \frac{\alpha c}{C_v}\overline{E^2} \tag{24}$$

and

$$\frac{\partial^2 \rho_1}{\partial t^2} \approx u^2 \beta \rho_0 \nabla^2 T_1 \,, \tag{25}$$

where T_1 is the local temperature excess, $T-T_0$. One must recall that the intensity, $c\overline{E^2}$, appearing in (24) is a function of time and position. Integrating (24) from zero to t and combining the resulting equation with (25) to eliminate T_1, one can obtain

$$\frac{\partial^2 \rho_1}{\partial t^2} \approx v_s^2 \frac{\beta \alpha I_L}{c C_p}\left(\frac{32 z_0}{r_0^2}\right)\exp\left[-8\left(\frac{r}{r_0}\right)^2\right] \times \left(\frac{8r^2}{r_0^2}-1\right)\int_{z-ct}^{z} \exp\left[-8\left(\frac{\nu}{z_0}\right)^2\right]\frac{d\nu}{z_0} \,. \tag{26}$$

It is straightforward to integrate this expression and, although the details will not be given here, it is clear that ρ_1 will have the form

$$\rho_1 \approx \left[\left(\frac{8r^2}{r_0^2}-1\right)\exp\left(-\frac{8r^2}{r_0^2}\right)\right] F(z,t) \,, \tag{27}$$

so that $\rho < \rho_0$ on axis and there is an off-axis maximum in the density. In other words, there will be a pile up of the fluid at a distance $r \approx \frac{1}{2} r_0$ from the axis.

The temperature distribution can easily be obtained by integrating (24) from zero to t:

$$T_1 \approx \frac{z_0 \alpha I_L}{c \rho_0 C_v}\exp\left(-8\frac{r^2}{r_0^2}\right)\int_{z-ct}^{z} \exp\left[-8\left(\frac{\nu}{z_0}\right)^2\right]\frac{d\nu}{z_0} \,. \tag{28}$$

A negligible term involving ρ_1 can be evaluated using (27) and has been dropped to obtain (28).

Combining (27) with (23) the behavior of E_1 can be visualized and studied analytically. Closed contours such as those shown in Fig. 9 are predicted and other qualitative features are correct. A detailed comparison of this analytical procedure and the computer result is in progress and it is now clear that striking quantitative agreement is obtained. This success is of great interest because the analytic procedure, unlike the present computer solution, is not limited to 10^{-5} sec. For the present, however, only the computer solution is presented.

V. RESULTS OF THE COMPUTATION FOR THE STATE OF THE FLUID

Analysis of the computer result for the state of the fluid at $t=10^{-5}$ sec will now be considered. For this discus-

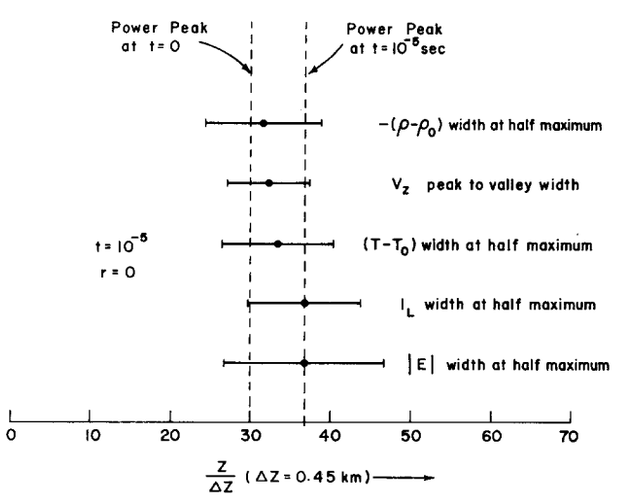

FIG. 17. Location and full $1/e$ widths of the various laser and fluid pulses are shown vs z. The peak-to-valley distance is shown for v_z. The initial and final locations of the laser power peak are also indicated.

Downloaded 14 Sep 2009 to 163.13.32.114. Redistribution subject to AIP license or copyright; see http://jap.aip.org/jap/copyright.jsp

sion, it is useful to keep several characteristic distances in mind. Since the state of the fluid is governed by the intensity profile

$$I_L(r,z,t) \equiv \tfrac{1}{2}(\epsilon_{0e})^{1/2} c\,|E|^2, \tag{29}$$

rather than by $|E|$ directly, the following initial parameters are relevant: The full $1/e$ width of the z profile of the intensity is

$$z_0/\sqrt{2} = 14.1 \quad \text{in units of } \Delta z \equiv 0.45 \text{ km}. \tag{30}$$

At $z = z_p \pm \tfrac{1}{4}z_0 = z_p \pm 5$,

$$\frac{\partial^2 I_L}{\partial z^2} = 0 \tag{31}$$

so that $\partial I_L/\partial z$ has extrema separated by 10 units. The full $\frac{1}{e}$ width of the radial intensity profile is

$$r_0/\sqrt{2} = 0.707 r_0 = 141 \text{ cm}. \tag{32}$$

At $r = \tfrac{1}{4}r_0 = 50$ cm,

$$\frac{\partial^2 I_L}{\partial r^2} = 0\,, \tag{33}$$

so that $I_L/\partial r$ has a maximum. The maxima on opposite sides of the axis (diameter of the density doughnut) are separated by 100 cm.

The local temperature excess $T - T_0$, where $T_0 = 10\,^{\circ}\text{C}$, is shown in Fig. 10 as a function of z at $t = 10^{-5}$ sec. This curve is in complete quantitative agreement with the analytical result shown in (28). The hottest place in the beam lies on the axis at $z \approx 33.3$. Since the intensity peak is at $z_p \approx 35.3$, it is clear that the thermal peak is lagging behind the intensity peak. Since $z_c \approx 36.6$ at this time, it is clear that the thermal peak is almost exactly midway between the initial and final pulse centers. Thus one finds, as expected, that the thermal peak propagates at velocity $\frac{1}{2}c$ for small times. This and other properties of the thermal profile are readily understood on the basis of the following considerations. The temperature responds to the heat deposited in the medium, so that from (28),

$$T(z) - T_0 \approx \int_{z-(z_p-z_{p0})}^{z} \left(\frac{\alpha}{\rho_0 C_v} I_L(r,z',t=0)\frac{dz'}{c}\right). \tag{34}$$

Due to the symmetry of I_L and the fact that it is Gaussian, it follows from (34) that $T(z)$ should reach a maximum midway between z_{p0} and z_p for small times. Furthermore, the graph of $T(z) - T_0$ should be symmetric about its maximum. Both of these features are evident in Fig. 10. Since the peak moves much less than its half-width in 10^{-5} sec, the integrand in (34) is essentially constant. Evaluating $I_L(r,z',t)$ at the midpoint of the interval, one obtains

$$T(z) - T_0 \approx [(z_t - z_{p0})/c](\alpha/\rho_0 C_v) I_L(r, z - \tfrac{1}{2}(z_p - z_{p0}),\ t=0). \tag{35}$$

From (35) one concludes that the width of the thermal distribution should equal the width of the intensity distribution. Indeed, one sees in Fig. 10 that the temperature distribution has a width 14.1, which is to be compared with (30).

The corresponding radial temperature distribution at $z = 33$, the position of the maximum at $t = 10^{-5}$ sec, is given in Fig. 11. This curve, also, is in complete quantitative agreement with the analytical result shown in (28). The temperature has reached a maximum of more than 1000 °K on axis and the full width of the distribution is found to be $0.67 r_0 = 134$ cm, 5% narrower than the initial radial intensity width. One might have expected the temperature distribution to be broader than the intensity profile because the large radial velocity of the fluid should carry some of the deposited energy away. In fact, this effect may possibly be observed in the following way. One might compare the temperature distribution not to the original Gaussian intensity profile, but rather to the $1/e$ width of the radial intensity profile at $t = 10^{-5}$ sec. This final intensity profile has a width of 128 cm or 5% less than the temperature width. The average of the two intensity widths is 134.5 cm, almost exactly the observed temperature width. This average may be the best measure, becuase the thermal peak is midway between the initial and final intensity peaks.

The z component v_z of the fluid velocity is shown in Fig. 12 as a function of z. A double log plot is used which omits values of v_z between 10^{-3} and -10^{-3} cm/sec. This kind of plot allows negative values of v_z to be plotted below the "axis". The zero of the velocity distribution occurs around $z = 32.2$, so the "center of velocity" lags slightly behind the thermal maximum. From the differential equation for v_z, one might expect to find

$$v_z \sim \frac{\partial T}{\partial z} \sim \frac{\partial I_L}{\partial z}\,, \tag{36}$$

so that the peaks in Fig. 12 would be separated by 10 units according to (31). Indeed, the peaks are found to be separated by 10.2 units. Furthermore, since the temperature curve is symmetric about its maximum, (36) would suggest that v_z should be antisymmetric about its zero. This effect is correctly observed in Fig. 12. The velocity distribution is delayed with respect to the temperature distribution, but this symmetry property is unaffected.

At the same value of z, corresponding to the center of velocity of the z component, the radial component v_r is plotted in Fig. 13. This value of z corresponds also to the largest radial velocities, so that $z = 32$ might also be termed the site of greatest kinetic energy in the fluid. The radial velocity maximum is 4600 times larger than the maximum axial velocity. This effect arises because of the great disparity in the intensity widths in the two directions. As a matter of fact,

$$\frac{(v_r)_{\max}}{(v_z)_{\max}} = 4625 \quad \text{and} \quad \frac{z_0}{r_0} = \frac{9\times 10^5}{200} = 4500\,.$$

The curve of v_r is forced to go to zero, as r goes to zero, by the boundary conditions shown in (5). One notes, however, that the peak is located at the distance $0.25 r_0$ from the axis, exactly the location of the maximum of $\partial I_L/\partial r$ shown in (33). Thus one finds

$$v_r \sim \frac{\partial I_L}{\partial r} \sim \frac{\partial T}{\partial r} \tag{37}$$

Downloaded 14 Sep 2009 to 163.13.32.114. Redistribution subject to AIP license or copyright; see http://jap.aip.org/jap/copyright.jsp

as would be expected from the differentail equation for v_r.

Bringing up the rear in the sequence of effects is the density minimum at $z \approx 31.5$. The density decrement $-(\rho - \rho_0)$ is shown in Fig. 14. Using (25), one might expect

$$\frac{\partial^2 \rho}{\partial t^2} \sim \frac{\partial^2 T}{\partial r^2} \ , \tag{38}$$

so that ρ and T will have the same z dependence.[4] There should, however, be a double time delay, since two time integrations are indicated in (38). The width of the density decrement is found to be 14.5, about 3% wider than the thermal and intensity widths. The maximum fractional decrement $(\rho_0 - \rho)/\rho_0 \approx 4 \times 10^{-5}$.

The radial density distribution is exhibited in Fig. 15 at $z = 32$, the location of the density minimum in the z profile. Again, a double log plot is given so that both positive and negative density excesses can be conveniently represented. This time a density pile up is observed because the fluid has been blown away from the axis so fast that a compression wave is generated. The zero in the graph is at $0.36 r_0$, right at the half-widths of the thermal and intensity distributions. Thus inside the thermal half-width the density is depressed; outside the fluid has piled up. The radial density profile shown in Fig. 15 is in excellent agreement with that predicted in (27). For example, the zero observed at $r/r_0 \approx 0.36$ is predicted to occur at

$$r/r_0 = 1/\sqrt{8} = 0.354.$$

Similarly, the location of the peak observed at $r/r_0 \approx 0.51$ is predicted to occur at

$$r/r_0 = \tfrac{1}{2}.$$

Similarly, the ratio of peak height to valley depth is also correctly predicted. As a matter of fact, when one takes the trouble to evaluate the function $F(z, t)$ appearing in (27), he finds precise agreement between (27) and Fig. 15. Thus, both (27) and (28) are in complete quantitative agreement with the result of the computer calculation.

Figures 16 and 17 exhibit the parade of effects, illustrating graphically the various delays, pulse shapes, and widths. Physically the delays make sense. First the beam blasts through, heating the fluid as it passes. As explained above, the temperature maximum moves at $\frac{1}{2}c$ and, thus, behind the laser peak. As this temperature wave passes along, the fluid picks up kinetic energy and the flow velocities increase. The center of this effect trails the heat wave, allowing time for the fluid to respond. Then, as the fluid begins to flow away from the propagating center of velocity, density deficits are left in the wake and corresponding radial compression waves set out from the beam axis.

VI. SUMMARY OF RESULTS

In portions of the pulse where the intensity is small, there is very little interaction with the fluid and these portions move without appreciable distortion. The peak of the pulse, however, interacts fairly strongly with the fluid and the peak is delayed relative to the center of the pulse. A parade of effects ensues; the center and edges of the pulse are followed by the peak, which, in turn, is followed consecutively by the thermal wave, the center of velocity, and the density waves. The front edge of the pulse propagates without appreciable distortion, but strong phase oscillations are set up near the peak and rapidly overtake the undistorted front section indicating that soon the entire beam will be distorted to some degree. The strongest instabilities predicted in the linearized analysis of Ref. 1 could not appear in the computer solution because they are generated by ripple with wavelength an order of magnitude smaller than the mesh size used. The success of the analytic analysis presented here suggests, however, that such instabilities are not important for the time interval considered.

There is very little hope of obtaining computer solutions of the laser-fluid equations except in the tightly limited regime reported here, unless a different calculational procedure can be devised. Since, however, it appears that a certain amount of analytical headway has been made, there is reason to believe that, with appropriate combination of analytical and computer methods, the beam can be followed for considerably longer periods of time. Effort is currently being directed toward this objective.

*Research supported by Advanced Research Projects Agency of the Department of Defense and monitored by the Office of Naval Research under Contract No. N00014-67-A-0269-0006.

[1] J. D. Reichert, W. G. Wagner, and W. Y. Chen, preceding paper, J. Appl. Phys. **44**, 3641 (1973). Instabilities of the Brueckner–Jorna type are considered as well as a new class of instabilities arising from beam-driven turbulence.

[2] Some of the groups that have developed sophisticated propagation codes are listed in Ref. 8 of Ref. 1.

[3] W. Y. Chen, J. D. Reichert, and W. G. Wagner, Mathematics of Computation (to be published).

[4] One gets the same conclusion by analyzing the function $F(z,t)$ shown in (27) in a manner analogous to the reasoning employed to obtain (35).

Downloaded 14 Sep 2009 to 163.13.32.114. Redistribution subject to AIP license or copyright; see http://jap.aip.org/jap/copyright.jsp